AGU PUBLICATIONS

JGR

Journal of Geophysical Research: Solid Earth

RESEARCH ARTICLE
10.1002/2014JB011220

Key Points:
- Stick slips on saw-cut fault in granite initiate as acoustic emission event
- Maximum magnitude of acoustic emission controlled by fault roughness
- Cascade of acoustic emission to stick slip facilitated by aseismic preslip

Supporting Information:
- Readme
- Figure S1
- Figure S2
- Figure S3
- Figure S4
- Figure S5
- Figure S6
- Figure S7
- Figure S8
- Figure S9

Correspondence to:
G. C. McLaskey,
gmclaskey@usgs.gov

Citation:
McLaskey, G. C., and D. A. Lockner (2014), Preslip and cascade processes initiating laboratory stick slip, *J. Geophys. Res. Solid Earth*, *119*, 6323–6336, doi:10.1002/2014JB011220.

Received 21 APR 2014
Accepted 3 JUL 2014
Accepted article online 9 JUL 2014
Published online 1 AUG 2014

Preslip and cascade processes initiating laboratory stick slip

Gregory C. McLaskey[1] and David A. Lockner[1]

[1]United States Geological Survey, Menlo Park, California, USA

Abstract Recent modeling studies have explored whether earthquakes begin with a large aseismic nucleation process or initiate dynamically from the rapid growth of a smaller instability in a "cascade-up" process. To explore such a case in the laboratory, we study the initiation of dynamic rupture (stick slip) of a smooth saw-cut fault in a 76 mm diameter cylindrical granite laboratory sample at 40–120 MPa confining pressure. We use a high dynamic range recording system to directly compare the seismic waves radiated during the stick-slip event to those radiated from tiny (M −6) discrete seismic events, commonly known as acoustic emissions (AEs), that occur in the seconds prior to each large stick slip. The seismic moments, focal mechanisms, locations, and timing of the AEs all contribute to our understanding of their mechanics and provide us with information about the stick-slip nucleation process. In a sequence of 10 stick slips, the first few microseconds of the signals recorded from stick-slip instabilities are nearly indistinguishable from those of premonitory AEs. In this sense, it appears that each stick slip begins as an AE event that rapidly (~20 μs) grows about 2 orders of magnitude in linear dimension and ruptures the entire 150 mm length of the simulated fault. We also measure accelerating fault slip in the final seconds before stick slip. We estimate that this slip is at least 98% aseismic and that it both weakens the fault and produces AEs that will eventually cascade-up to initiate the larger dynamic rupture.

1. Introduction

It is not known whether earthquakes begin as small dynamic instabilities that rapidly grow into larger ruptures or as slow but accelerating aseismic fault slip that eventually reaches a critical size R_C and then transitions to dynamic rupture. These two end-member models are termed the "cascade" model and "preslip" model, respectively [*Ellsworth and Beroza*, 1995; *Beroza and Ellsworth*, 1996]. *Noda et al.* [2013] recently studied a numerical model that combines elements of both. Based on the work by *Ide and Aochi* [2005] and *Lapusta and Liu* [2009], Noda's model includes small brittle patches embedded in a larger fault patch with higher overall toughness. The small patches have small R_C and can rupture dynamically to produce small earthquakes. The larger patch has larger R_C and will initiate a larger earthquake either with (1) an extended nucleation period (large preslip), or (2) rupture of a small patch which directly triggers rupture of the larger patch in a dynamic "cascade-up" process. If such a cascade-up behavior is a common feature of natural faulting, it might explain the lack of a detectable aseismic nucleation phase in the days to weeks prior to earthquakes [e.g., *Roeloffs*, 2006].

We have conducted laboratory experiments that we believe are somewhat analogous to the multiscale model of *Noda et al.* [2013]. We show that tiny acoustic emission events, described below, result from the dynamic rupture of smaller brittle patches, and that these events interact with the nucleation of larger dynamic instabilities which occur on the simulated fault. In this paper, we refer to these instabilities as dynamic slip events (DSEs).

DSEs are often called "stick slips," and they are thought to be analogous to earthquakes [*Brace and Byerlee*, 1966]. DSEs are associated with measureable fault slip, sudden drops in the stress supported by the sample, and intense radiation of seismic waves. Piezoelectric sensors glued to the sample measure the mechanical vibrations produced by DSEs. This information has been used to study the initiation of stick slip [*Thompson et al.*, 2005], rupture velocity [*Passelègue et al.*, 2013], and fault healing [*McLaskey et al.*, 2012].

On a smaller scale, acoustic emissions (AEs) are brief bursts of vibrations a few tens of microseconds in duration. AEs are not typically associated with externally measureable fault slip or drops in stress. They are thought to be the result of rapid stress redistribution likely caused by microcracking or slip instability on the grain scale [*Lockner*, 1993]. AEs tend to cluster around DSEs in a manner reminiscent of foreshocks and aftershocks, and they often

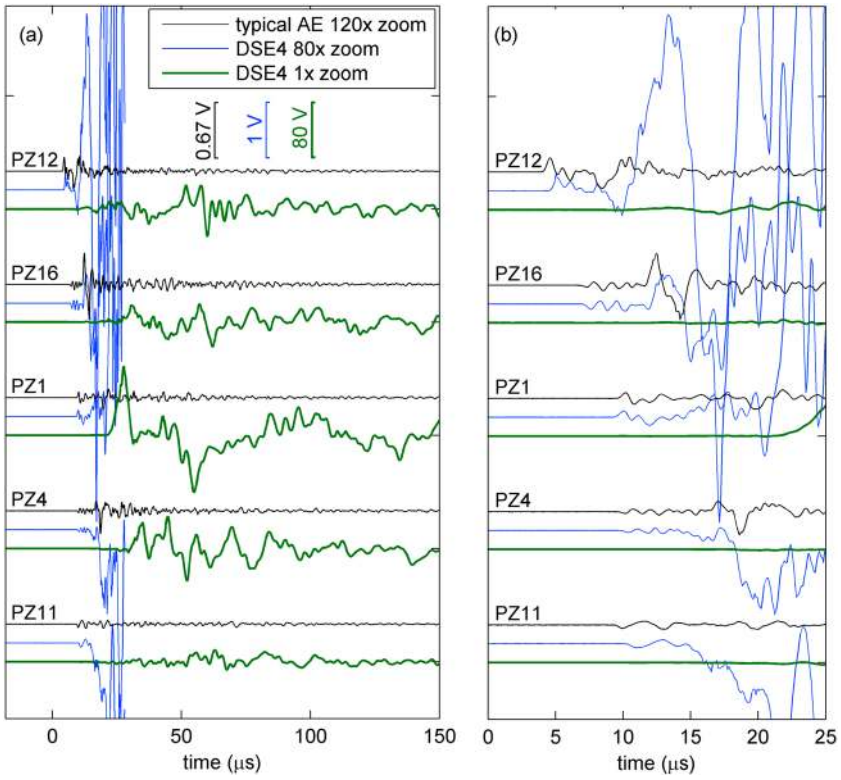

Figure 1. (a, b) Signals from the initiation of a stick-slip instability (DSE4) recorded by 5 of the 16 piezoelectric sensors (PZ1–PZ16). The thick green lines show the DSE signals on scale. Blue lines are a zoom in on the weak-but-abrupt initiation of the DSE (for clarity, only the first 25 μs are shown). These are shown alongside signals from a "typical" AE (black lines) which was similar sized and occurred in a similar location on the fault 1.5378 s before DSE8. The first arrivals are shown at greater time magnification in Figure 1b. In the first 5–10 μs, signals from the initiation of the DSE are essentially indistinguishable from those of the AE.

obey both Gutenberg-Richter frequency-magnitude statistics and Omori-type aftershock decay [*Goebel et al.*, 2012; *Lei*, 2012; *Weeks et al.*, 1978]. It has been assumed that both AEs and DSEs are in some sense small-scale versions of earthquakes and can provide insights into earthquake mechanics [e.g., *Lei et al.*, 2003; *Thompson et al.*, 2009; *Johnson et al.*, 2013; *Goebel et al.*, 2014a, 2014b].

Despite the many similarities, there are also significant differences between natural earthquakes and laboratory-generated DSEs and AEs. For example, DSEs rupture the entire simulated fault surface, and therefore, they feel the sample boundaries and are affected by the stiffness of the loading frame [e.g., *McGarr*, 2012]. Most natural earthquakes are entirely embedded within the host rock. While AEs emanating from the center of the sample are not affected by the boundaries, it is not clear whether their small size relative to grain size causes their physics to diverge from that of larger earthquakes. For example, AEs produced from intact rock samples without a preexisting fault are the result of microcrack growth due to grain-scale stress heterogeneity [*Lockner*, 1993]. This introduction of a specific length scale probably has no counterpart for natural earthquakes. On the other hand, AEs produced on a saw-cut surface may be less affected by grain size and more controlled by the fault surface roughness.

Additionally, the analysis of AEs and DSEs often falls short of standard earthquake analyses. For example, in most studies, the absolute sizes of AEs are not known, so it is difficult to link them to a specific physical process. Also, DSEs are so energetic that the large-amplitude seismic waves that they generate commonly saturate the recording system, so their amplitudes and durations are also not known.

Similar to previous studies, we study sequences of DSEs and AEs occurring on well-defined saw-cut simulated faults in cylindrical granite samples at 40–120 MPa confining pressure. Earlier studies reported that DSEs initiate abruptly, and the hypocenter could be located by standard arrival time inversion techniques [*Thompson et al.*, 2005; *Passelègue et al.*, 2013]. Here we show that the weak-but-abrupt beginning of the DSEs is nearly indistinguishable from standard AEs and can be interpreted as an AE that rapidly (~20 μs) grows

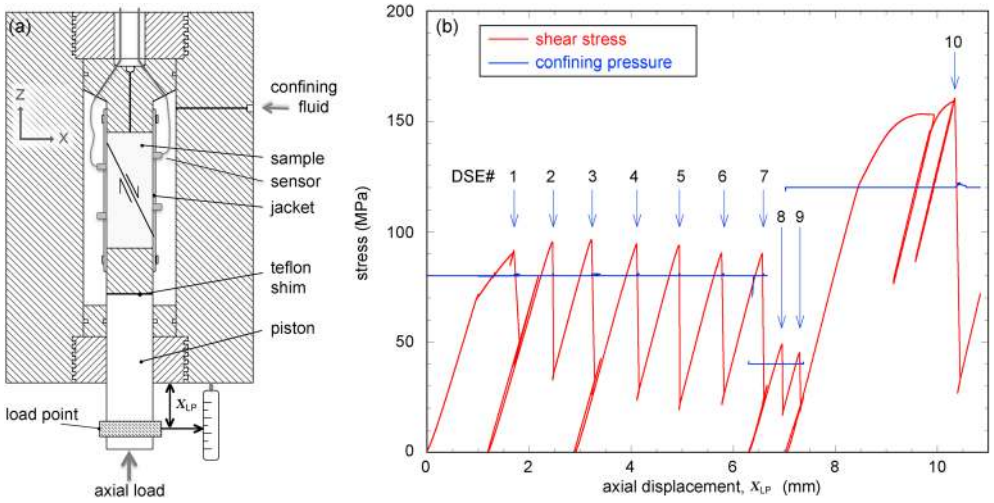

Figure 2. (a) Schematic diagram of the 76 mm diameter cylindrical granite sample inside the pressure vessel of the triaxial loading apparatus. The sample has a precut fault oriented 30° from the loading axis (*z* direction), and the slip direction is marked with arrows. (b) Loading curves for the set of 10 dynamic slip events (DSEs) conducted at confining pressures of 80 MPa, 40 MPa, and 120 MPa. Each DSE is characterized by a rapid drop in shear stress at constant axial displacement. Acoustic emissions (AEs) were detected in the seconds to milliseconds prior to each DSE. Note that just prior to DSE10 the loading piston was retracted and then advanced at a higher load point velocity in order to induce stick-slip behavior rather than steady sliding.

about 2 orders of magnitude in size and ruptures the entire 150 mm length of the simulated fault. Consequently, we term the weak-but-abrupt beginning of a DSE (i.e., the hypocenter) a DSE-initiating AE. In a unique aspect of this study, we have recorded, on scale, the full waveforms of the seismic waves associated with DSEs as well as precursory AEs at high resolution. This allows us to carefully analyze the similarities and differences between DSE-initiating AEs that grow large and AEs that do not. Examples of AE and DSE signals are shown in Figure 1 and Figure S1 in the supporting information.

The purpose of this paper is to study DSEs and AEs in detail, describe the conditions under which DSEs initiate, and determine the role that AEs play in the process. The relatively large (76 mm diameter) sample size and 16-sensor AE system allow us to perform detailed analyses, and we describe the locations, amplitudes, and focal mechanisms of both typical AEs and DSE-initiating AEs. We also analyze the source spectra of AEs and DSEs in the 5 kHz to 1.5 MHz frequency band. Unlike nearly all other AE studies, we are able to quantify the seismic moments and estimate the size and stress drops of the AE using a ball impact empirical calibration procedure that is reported elsewhere (G. C. McLaskey et al., A robust calibration technique for acoustic emission systems based on momentum transfer from a ball drop, submitted to *BSSA*, 2014). Finally, we discuss our observations in light of preslip and cascade earthquake models, and we argue that while a cascade process does occur, it is facilitated by aseismic preslip due to a larger nucleation process.

2. Experimental Procedure

Tests were performed on a cylindrical sample of Westerly granite 76.2 mm in diameter and 175 mm long loaded in a triaxial apparatus as depicted in Figure 2a. The sample has a saw cut inclined at 30° to the vertical axis to simulate a fault. The saw-cut surfaces were surface ground and then hand lapped with 600 grit abrasive (approximately 15 μm particle size) to produce a smooth uniform surface. The sample was mounted between steel end pieces and placed in a 4.8 mm wall thickness polyurethane sleeve to isolate it from the confining fluid (silicone oil). The sample was instrumented with an array of 16 piezoelectric sensors. Each sensor consisted of a cylindrical piezoceramic element (piezoelectric lead zirconate titanate) 6.35 mm in diameter and 2.54 mm thick that was soldered inside a brass cup. The bottom of the brass cup was machined to match the sample curvature and was glued directly on the granite sample through predrilled holes in the polyurethane sleeve. The sample assembly was loaded into the pressure vessel and constant confining pressure p_c of 40, 80, or 120 MPa was applied during the test sequence as illustrated in Figure 2b. Axial stress σ_1 was applied with a hydraulic ram that advanced a steel piston against the bottom of the sample column (Figure 2a). A greased Teflon shim (0.13 mm thick) was placed between the piston and the steel end piece to

Table 1. Properties of the 10 DSEs[a]

	p_c	v_{LP}	$(x_{LP} - \tau/k)/\cos(30°)$	$\Delta\delta$	τ_{max}	$\Delta\tau = \tau_{max} - \tau_{min}$	A_0 (DSE-Initiating AE)	Total AE $> A_{complete}$	M_0	Inferred Preslip
	(MPa)	(μm/s)	(mm)	(mm)	(MPa)	(Mpa)	(V)		(Nm)	(μm)
DSE1	80	1	0.81	0.67	91.5	40.8	>10	1	0.1	1
DSE2	80	0.2	1.63	0.79	95.2	47.8	0.1–0.5	n/a	n/a	n/a
DSE3	80	0.2	2.52	0.87	94.5	52.2	0.5–2.5	n/a	n/a	n/a
DSE4	80	0.5	3.50	0.90	94.5	54.3	4	12	1	6
DSE5	80	0.5	4.47	0.94	93.8	57.0	2	9	1	4
DSE6	80	0.5	5.46	0.89	90.3	52.5	0.5	16	3	6
DSE7	80	0.5	6.40	0.87	90.2	52.4	2	22	3	6
DSE8	40	1	7.14	0.42	49	24.8	1	73	34	9
DSE9	40	1	7.57	0.35	45.2	20.5	~4	>73	>13	10
DSE10	120	10	9.99	1.76	160.7	104	1	19	11	?

[a]Column descriptions from left to right: DSE name, imposed confining pressure, imposed load point displacement rate, cumulative fault slip just prior to the DSE, fault slip during the DSE, shear stress resolved on the simulated fault just prior to the DSE, change in shear stress resolved on the fault during the DSE assuming that unloading stiffness is equal to loading stiffness, amplitude of the DSE-initiating AE, total number of precursory AEs above completeness threshold $A_{complete}$, cumulative M_0 of those events assuming $M_0 = \alpha A_0$, and $\alpha = 0.22$ Nm/V, inferred fault slip in the final 20 s prior to the DSE as described in section 3.5.

accommodate lateral motion of the lower sample half in response to slip on the inclined fault surface. For this axisymmetric test geometry, $\sigma_2 = \sigma_3 = p_c$. Then, shear and normal stresses resolved on the fault surface were computed according to $\tau = \frac{1}{2}(\sigma_1 - \sigma_3))\sin(60°)$ and $\sigma_n = \frac{1}{2}((\sigma_1 + \sigma_3) - (\sigma_1 - \sigma_3)\cos(60°))$. As slip on the fault surface accumulates, the contact area on the fault decreases, and the relative position of transducers on the sample halves changes. These effects were accounted for in reporting stresses and in locating AE sources.

Axial displacement, x_{LP}, and axial stress, σ_1, were measured outside the pressure vessel at the position identified as "load point" in Figure 2a. Displacement was measured with a direct current displacement transducer and refers to motion of the piston relative to the base of the pressure vessel. Consequently, x_{LP} includes both fault slip and elastic distortions of the vessel and sample column in response to changes in stress. Fault slip δ is not measured directly but can be approximated by subtracting the elastic shortening of the sample column from the total axial displacement $\delta = (x_{LP} - \tau/k)/\cos(30°)$ (see section 3.5 for a discussion of apparatus stiffness k). The seal friction (approximately 1% of the confining pressure) was measured before the piston contacted the sample and was removed from the axial stress measurement. Since all tests were performed with the piston advancing, uncertainties in σ_1 from changes in seal friction were minimized. Load point position was computer controlled using a fast-acting servo valve. Axial stress was applied by imposing a constant axial shortening rate $v_{LP} = d(x_{LP})/dt$. Confining pressure was also computer controlled and adjusted once every second. Axial displacement was updated 5 times per second. σ_1, p_c, and x_{LP} were recorded at 1 Hz sampling rate. Precision in measuring stresses and displacement are ±0.05 MPa and ±0.0005 mm, respectively.

Signals from the 16 piezoelectric sensors (PZ1–PZ16) were split and digitized (14 bit, 10 MHz) at two different gain settings 60.7 dB apart, denoted high resolution (26 dB) and low resolution (−34.7 dB). All voltages reported in this paper are voltage produced by the sensors prior to amplification. Using this split-gain recording mode with an effective dynamic range of 116 dB, we are able to directly compare tiny AE signals (~10 mV signal amplitude) with the largest DSE signals (~200 V) (see Figure 1).

Blocks of high-speed data 45 ms long were recorded in a triggered mode which allowed for overlapping blocks such that signals from all 16 sensors were continuously recorded with no dead time as long as the output from at least one of those sensors exceeded the ±35 mV threshold. No high-pass filters were employed. Our goal was to capture wide-band records of all of the seismic radiation associated with DSEs and the largest premonitory AEs.

3. Results

3.1. General Observations

In rock friction experiments, sample behavior depends upon the stiffness of the loading apparatus. Loading machines stiffer than a critical stiffness k_{crit} will produce stable sliding, and those more compliant than k_{crit} will reliably produce DSEs (stick slips) [*Dieterich*, 1978; *Ruina*, 1983]. Machines which operate close to k_{crit} produce a more varied and less predictable response [e.g., *Baumberger et al.*, 1994]. In the current experiments, we observe both quasi-stable slip and DSEs, so we believe that we are operating relatively close

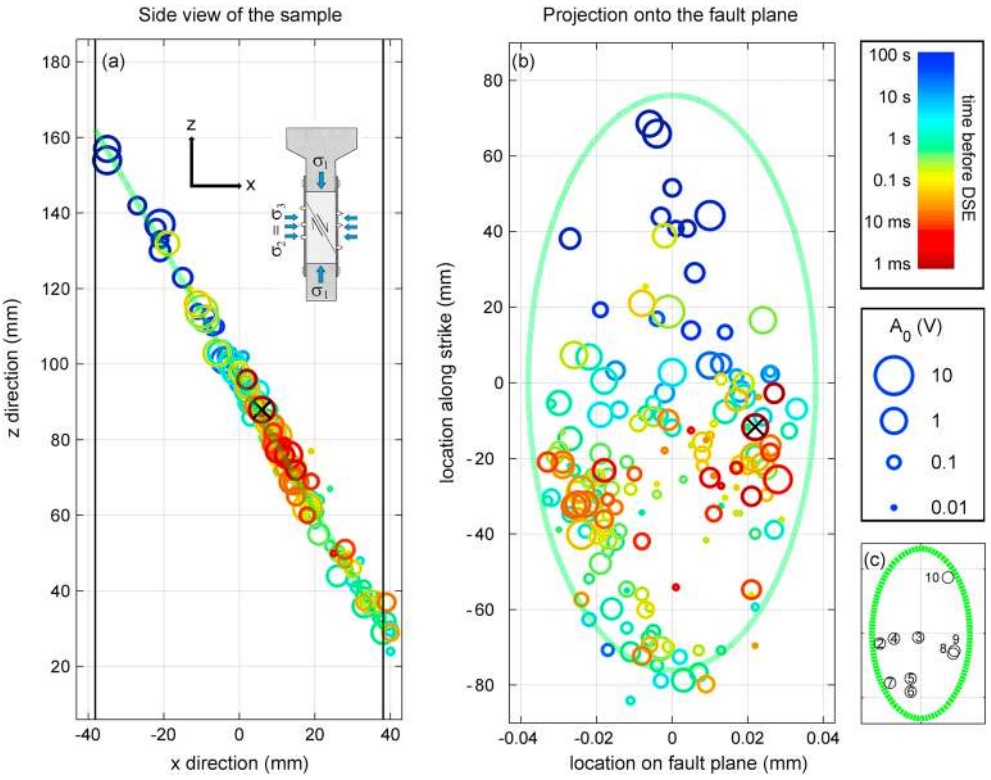

Figure 3. Locations, sizes, and timing of premonitory AEs that occur prior to DSE8. Circle size indicates the AE size. This catalog is complete down to $A_0 = 0.2$. Color indicates the timing of the AEs relative to the initiation of DSE8. (a) Side view of the sample shows that AE locations roughly lie on the plane of the simulated fault (green dashed line). Sample configuration in the apparatus is shown in the inset. (b) AE locations are shown projected onto the fault plane. The AE marked with a black cross is the DSE-initiating AE which grows into the complete rupture of the simulated fault and produces DSE8. (c) The locations of DSE-initiating AE from DSE2 to DSE10 are shown projected onto the fault plane.

to k_{crit}. Stiffness of the loading frame is quantified in section 3.5. We performed a sequence of 10 stick slips (DSE1–DSE10) on the saw-cut fault (Figure 2b). Details are reported in Table 1. In some cases, a faster loading rate was required to force the sample to produce a DSE, otherwise it would only slide quasi-stably, particularly at low-confining pressure (DSE8–9) and at large cumulative fault slip (DSE10).

In general, we find a correlation between inferred slip rate and the rate of occurrence of AEs. If the fault slides slowly ($<v_{LP}$), AE occur sporadically or none are detected at all. If fault slip rate increases, a burst of AEs occurs. We recorded tens to hundreds of AEs in the seconds to milliseconds preceding most DSEs. These AEs are likely caused by an increase in the rate of predominantly aseismic slip that occurs during this time as described in section 3.5. DSEs conducted at lower confining pressure produced more premonitory AEs and more preslip. In general, the number of AEs and cumulative moment of the AEs correlates with inferred slip rate (see Table 1), but, as described in section 4.2, we find that AEs account for less that 2% of this slip.

We also recorded the very large amplitude signals produced during each DSE. In previous studies, the recording system saturated for at least 5 ms during each DSE [*Thompson et al.*, 2009; *Goebel et al.*, 2012]. Our split-gain recording system did not saturate, and this allows us to study the amplitude and spectra of DSEs (section 3.3) and to search for immediate aftershocks. Despite this, we detect no aftershocks in these experiments. Peak signal amplitudes of DSEs often exceeded 100 V and occurred 20 to 50 μs after the *P* wave arrival of the DSE-initiating AE (Figure 1). This is in stark contrast to AE signals whose peak amplitudes (~1 V max) are typically the result of the direct *S* wave arrival which occurs in the first ~15 μs. Since we did not use high-pass filters, the signals recorded from the DSEs had good signal-to-noise ratio from about 1 kHz to 1.5 MHz. Intense, high-frequency seismic radiation (> ~500 kHz) associated with each DSE was produced for only about 40 to 50 μs, and this was observed on all channels (see Figure S2 in the supporting information).

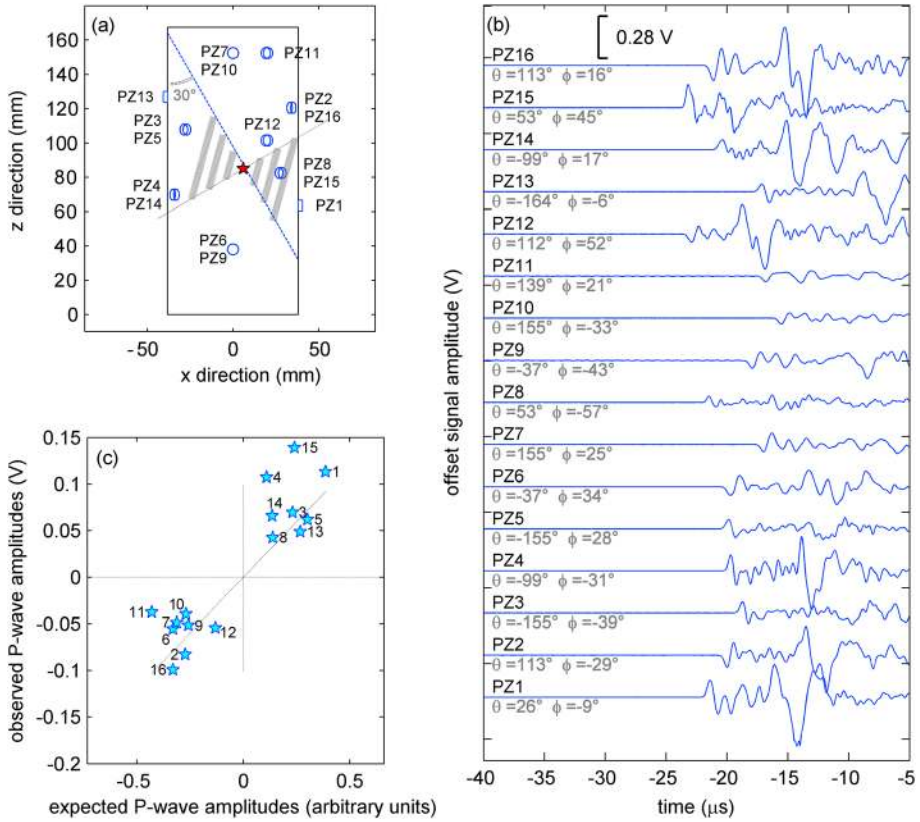

Figure 4. (a) The location of the 16 piezoelectric sensors (blue cylinders) relative to an AE source (red star). For a pure double-couple source, sensors located in the shaded quadrants should see compressional (up) first motions, and sensors located in the other two quadrants should see dilatational (down) first motions. (b) The AE signals recorded from the 16 sensors (PZ1–PZ16). Source-to-sensor takeoff angles θ, measured counterclockwise from the x axis in the x-z plane, and ϕ, measured counterclockwise from the x axis in the x-y plane, are also printed in light grey for each sensor. (c) For each of the 16 channels, the observed P wave amplitudes measured from the signals shown in Figure 4b are plotted against the expected P wave amplitudes based on a pure double-couple source aligned with the 30° simulated fault plane, shown in Figure 4a.

3.2. AE Locations

For each DSE, we located precursory AEs and DSE-initiating AEs by standard inversion of P wave arrival times, first picked automatically, but double checked by hand. The 3-D source location and origin time were found using a least squares inversion algorithm [*Mahajan and Walworth*, 2001]. Other inversion schemes [e.g., *Salamon and Wiebols*, 1974] produced similar results. Based on the amplitude and impulsiveness of P waves above the noise, we estimated that precision in P wave picking was <1 μs. Most events were located using picks from at least 12 sensors, and we estimate that the overall precision of source locations is ±2 mm.

Stress-induced anisotropy due to opening of microcracks is common in granite [*Stanchits et al*., 2003]. If an isotropic velocity model was used, an unreasonably high velocity was required for AE locations to align with the 30° angle of the saw-cut fault. Instead, we chose a velocity model with 9% radially symmetric anisotropy. Adding anisotropy made it possible to force the plane of AE locations to match the 30° saw-cut fault (to ±1.5° for DSE4–DSE10) while also keeping P wave velocities (6380 m/s in the fast (z) direction and 5800 m/s in the slow (x and y) directions) consistent with those reported in *Stanchits et al*. [2003]. A different choice of homogenous velocity model would shift the absolute AE locations but would have little effect on relative locations.

Figure 3 shows the locations, sizes, and timing of premonitory AEs that occurred prior to DSE8. The AE source locations form a plane, are broadly distributed over this plane, and there is some indication of migration over time. The locations, sizes, and timing of premonitory AEs that occurred prior to other DSEs are shown in Figures S3–S8 in the supporting information.

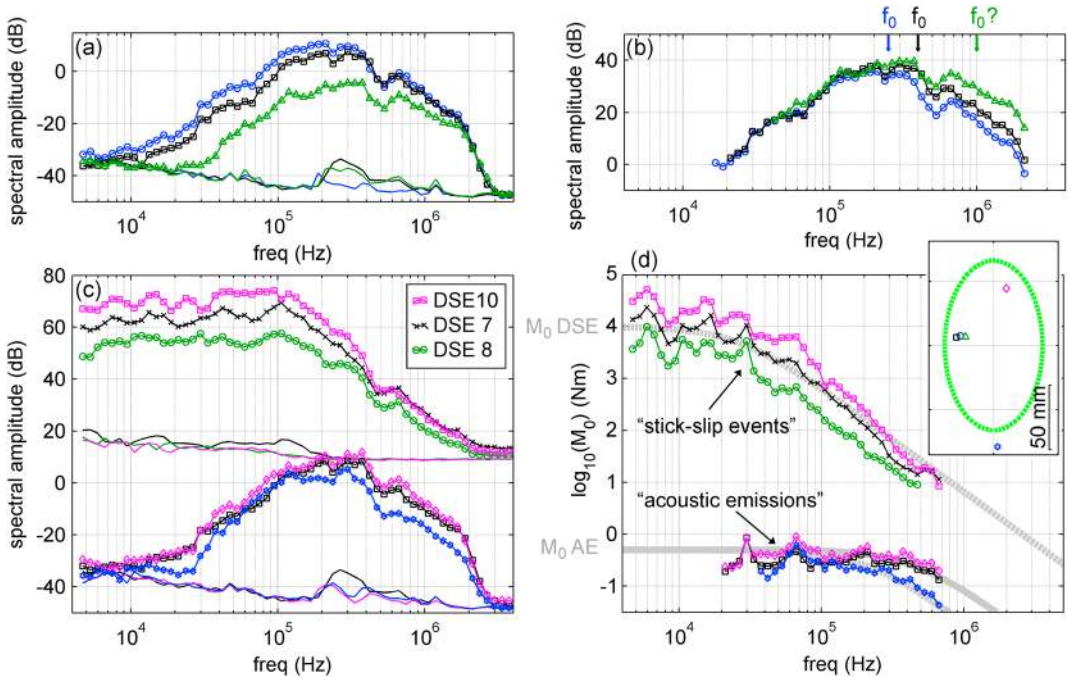

Figure 5. Spectra of AEs and DSEs derived from averages of spectra from at least 10 sensors' recordings. (a) Amplitude spectra of three collocated AEs (symbols) and associated noise spectra (lines). (b) The same spectra are shifted vertically to agree at low frequencies in order to illustrate spectral differences. (c) Spectra from three AEs that are not collocated are shown alongside the spectra of three DSEs. The noise level of the DSEs is larger because signals captured in the low-resolution gain setting were used. (d) The same spectra in Figure 5c are shown, but they are adjusted by the spectrum of an empirical calibration source that is believed to have a flat displacement spectrum (see text). This provides a rough estimate of the source spectrum of these events. The thick gray lines are *Brune* [1970] source models that approximately fit the data. The low-frequency level of the source spectra provides estimates of the moments M_0 of the AEs and DSEs. The inset shows the locations of the AEs (symbols) projected on the plane of the fault (green dashed oval).

3.2.1. Focal Mechanisms

We analyzed about 25 AEs of various sizes and found that the polarity and amplitudes of *P* waves radiated from the AEs are generally consistent with double-couple focal mechanisms with a nodal plane on the fault plane, as shown in Figure 4. This is consistent with previous work which showed that the largest AEs had predominantly deviatoric focal mechanisms [*Sellers et al*., 2003; *Thompson et al*., 2005, 2009].

3.3. Spectra of AEs and DSEs

For a single AE event, we observe some differences in spectra obtained from recordings from different sensors. Spectral differences are presumably due to differences in wave propagation effects such as increased attenuation for longer path lengths, geometrical spreading, radiation pattern of the source, and differences in instrument distortions such as a variation in sensor sensitivity with incidence angle. This sensor-to-sensor spectral variation can be as large as 20 dB at a given frequency, but by averaging spectra calculated from recordings from many different sensors, that encompass a variety of directions and path lengths, the spectral variation can be significantly reduced, resulting in a more stable estimate. Figure 5 shows spectra derived from averages of at least 10 sensors.

Amplitude spectra are obtained from the Fourier transform of 4.9 ms sections of the signals centered on the first wave arrival and tapered with a Blackman-Harris window [*Harris*, 1978]. This time window is long compared to the duration of both AEs and DSEs. It encompasses both direct arrivals and reflections, and it is necessary to provide stable spectral estimates down to 4.5 kHz. Figure 5a shows spectra of three AEs alongside noise spectra. These AEs (amplitudes are $A_0 = 1.3$, 1.0, and 0.3 V, see section 3.3) were chosen because we were able to obtain reliable spectral estimates in a relatively wide frequency band. In Figure 5b the same three spectra are offset vertically 25, 31, and 44 dB so that they agree at low frequencies. The AEs are

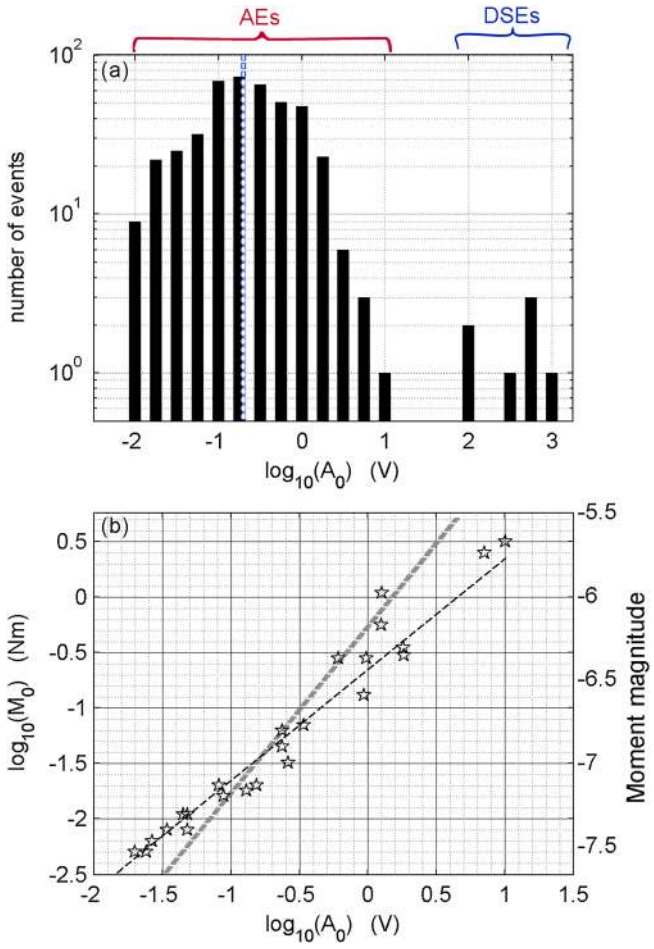

Figure 6. (a) Distribution of AE and DSE sizes. There is a clear gap between the largest AE ($A_0 = 10$ V) and the DSEs ($A_0 = 100$–1000 V). Our estimated completeness level is shown as a blue and white dashed line. (b) For 24 AEs of various sizes, we compare A_0 calculated from peak signal amplitudes to seismic moment M_0 calculated from low-frequency spectral levels (see section 3.4). The black dashed line has a slope of 1 indicating a linear relationship $M_0 = \alpha A_0$ and $\alpha = 0.22$ Nm/V. For reference, we also show $M_0 = \alpha_1 A_0^{3/2}$ (gray dashed line).

located within 5 mm of each other so we assume that differences between the spectra of these events are due to differences in the source, rather than wave propagation or sensor response. AE locations are near the left center of the fault as shown in Figure 5d (inset). Figure 5b shows that spectra of larger AEs contain less high frequency energy relative to low frequencies than those of smaller AEs. This is consistent with typical earthquake scaling behavior whereby earthquakes with larger seismic moments M_0 have lower corner frequencies f_0. We observe similar spectral differences between collocated AEs in other regions of the simulated fault. Figure 5b indicates that f_0 of the larger AE is about 200–300 kHz.

Figure 5c shows spectra from three similar-sized AEs and three DSEs. The three AEs are not collocated, but their spectral shapes are similar and vary by only 10 dB. This insensitivity to source location permits us to compare spectra of AEs to those of DSEs, which rupture the entire simulated fault. Figure 5d shows estimates of source spectra for the same events shown in Figure 5c. These are obtained by dividing raw spectral estimates (Figure 5c) by the spectrum of an empirical calibration source which has a flat displacement response spectrum in this frequency band. For frequencies between 80 kHz and 600 kHz, we use a small AE with $f_0 \sim 1$ MHz as the calibration source. For lower frequencies, where the small AEs have poor signal-to-noise ratio, we use a ball impact (McLaskey et al., submitted manuscript, 2014). Estimates are shown only in the frequency band with good signal-to-noise ratio.

As shown in Figure 5d, the AEs have roughly flat spectra in the 20–200 kHz range which indicates that their corner frequencies are above this band. The DSE spectra are not flat; their corner frequencies are below 20 kHz (50 μs minimum slip duration), and their high-frequency falloff is 40–50 dB/decade.

3.4. Amplitude and Seismic Moment of AEs

We first computed the amplitude A_0 of the AEs following *Zang et al.* [1998], based on the maximum amplitude of the signals scaled for geometrical spreading at a distance of 10 mm:

$$A_0 = \sqrt{\frac{1}{k}\sum_{i=1}^{k}\left(A_i \frac{r_i}{10}\right)^2},$$

where A_i is the maximum signal amplitude, and r_i is the source-to-sensor distance (in mm) for the ith of k sensors. This amplitude scale is advantageous because it is relatively easy to calculate, but it is specific to a particular type of sensor.

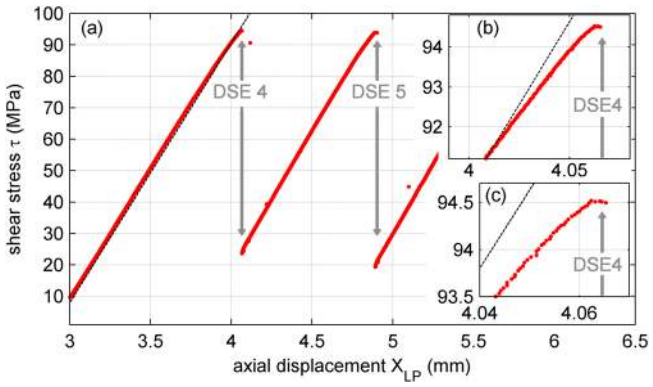

Figure 7. (a–c) Sudden drops in shear stress τ supported by the sample are associated with each DSE. When τ and x_{LP} vary linearly (black dashed line), we assume that the simulated fault is locked. Departure from linearity indicates premonitory fault slip prior to each DSE, as shown in the insets Figures 7b and 7c. Data are sampled at 10 Hz and averaged and then recorded at 1 Hz, and red dots indicate individual 1 Hz samples.

Based on our triggering threshold, we estimate the level of completeness $A_{complete} = 0.2$ V, as described in more detail in Figure S9 in the supporting information. We believe that we have faithfully recorded all AEs above this level. Figure 6a shows the distribution of A_0 for DSE4 to DSE10 and about 400 associated precursory AEs. $A_{complete}$ is marked with a blue and white dashed line.

We also estimated the seismic moment M_0 of the AEs based on spectral amplitude below f_0. Relative M_0 is equal to the offset required for spectra to overlay each other in the 50 kHz to 200 kHz frequency band, as shown in Figure 5b. Larger AEs with lower f_0 require a lower frequency band, to ensure that the comparison is made below f_0. Smaller AEs require a higher-frequency band to ensure adequate signal-to-noise ratio. Absolute M_0 is determined using a ball drop empirical Green's function (McLaskey et al., submitted manuscript, 2014). Based on the amplitude at the low-frequency limit of the source spectra (Figure 5d), we estimated that M_0 of the DSEs is about 1×10^4 Nm for DSEs conducted at 80 MPa confining pressure. In general, this low-frequency amplitude is proportional to the slip and measured stress changes during the DSE, which are in turn proportional to the confining pressure. (We estimate $M_0 = 4 \times 10^3$ Nm for DSE8 and DSE9 at 40 MPa and at least 3×10^4 Nm for DSE10 at 120 MPa; see Figure 5d.) Uncertainty in these estimates is the result of variability in individual spectral estimates, which is about ±9 dB.

Figure 6b shows a comparison between A_0 and M_0 calculated for 24 AEs with different sizes and locations. We find a linear dependence between A_0 and M_0 (i.e., a slope of 1 on the log-log plot) such that $M_0 = \alpha A_0^C$, where $C = 1$ and $\alpha = 0.22$ Nm/V. Some AE studies have assumed $C = 3/2$, which is consistent with earthquakes if it is assumed that magnitude $M = \log_{10}(A_0)$ [e.g., *Goebel et al.*, 2012]. Our results indicate that the relationship between f_0 and the frequency of peak sensor sensitivity can affect the relationship between M and A_0. For this study, peak sensitivity of the piezoelectric sensors is ~300–400 kHz (Figure 5a) which is at or below f_0 for most AE, and this results in $C = 1$. Note that because A_0 is specific to a particular sensor type, recording system, and sensor geometry, the above relation cannot be used to calculate M_0 for other AE tests. But since the M_0 is an absolute measurement, M_0 values obtained here are directly comparable to M_0 calculated on other apparatuses with different sensors and recording equipment [e.g., *McLaskey et al.*, 2014].

3.5. Acceleration of Inferred Slip Rate and AE Activity Prior to DSE

Figure 7 shows shear stress resolved on the precut fault, τ, plotted against load point displacement, x_{LP}, for DSE4 and DSE5. Below 70% of peak stress, we assume the fault surface is locked and the linear increase in stress with axial shortening provides a direct measure of machine stiffness $k = \Delta\tau/\Delta x_{LP}$, which varies slightly with confining pressure but is nominally 90 MPa/mm. When τ is close to peak stress, we observe that the slope of the τ versus x_{LP} curve decreases, which indicates precursory slip. Note that loading is controlled by imposing a constant v_{LP}, so premonitory slip causes the average stressing rate on the sample to decrease. In a stress versus displacement plot such as Figure 7, constant stress implies that fault creep is matching the applied displacement rate $d\delta/dt = v_{LP}/\cos(30°)$.

Figure 8 shows estimates of precursory slip rate $d\delta/dt$ derived from the first derivative of $\delta(t)$, smoothed with a 0.1 Hz causal low-pass filter to remove high-frequency noise. Remote loading rates are 0.5 to 1 μm/s, as reported in Table 1. The red line shows the cumulative number of AEs above $A_{complete}$ which occur in the seconds prior to each DSE. The circles on sticks show the amplitudes A_0 of the individual AEs on a log scale. DSE-initiating AE are filled red and have an *x*, and their amplitudes are estimated by comparing initial *P* wave amplitudes to collocated AEs with known A_0.

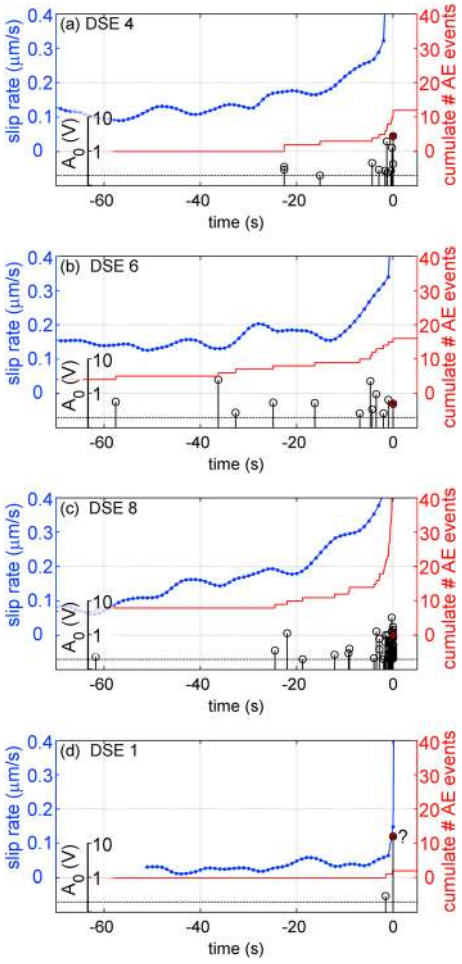

Figure 8. (a–d) Premonitory fault slip rate (blue), precursory AEs (black), and cumulative AE counts (red) are shown in the 70 s prior to four different DSEs. Time zero is the time of the DSE. Slip rate $d\delta/dt$ is derived from the first derivative of $\delta(t)$ and low-pass filtered at 0.1 Hz. For most DSEs, slip rate increases in the final 10 s prior to the DSE, and there is an increase in AE activity associated with this premonitory slip. DSEs appear to initiate as an AE that rapidly grows and ruptures the entire simulated fault surface. These DSE-initiating AEs are marked red and with a cross. In some cases (in Figure 8a) the DSE-initiating AE is the largest, but in other cases (in Figures 8b and 8c) it is not.

3.6. Initial *P* Wave Signature of DSEs

Figure 1 shows recorded signals associated with DSE4. A collocated AE of similar amplitude ($A_0 = 1.0$ V) is shown for comparison. The initial 5–10 μs of the both signals look very similar which indicates that in addition to being collocated, they have similar focal mechanisms and source time functions. After 5–10 μs, the waveforms of the DSE clearly diverge from the AE and in the subsequent ~20 μs grow about 2 orders of magnitude in amplitude to peak amplitudes between 30 and 150 V.

DSE2–DSE10 appear to initiate similarly to that shown in Figure 1 (see Figure S1 in the supporting information). Their first few microseconds appear similar to a typical AE with $A_0 = 0.5$–4 V. DSE-initiating AEs are among the largest AEs recorded ($M_0 \sim 0.1$–1 Nm). DSE1 was different from the rest. Only one precursory AE was detected despite lower (~3 mV) trigger threshold levels, and the DSE-initiating AE was much larger ($A_0 > 10$ V) than those of other DSEs, but we can only estimate the lower bound since we did not capture this first DSE on scale. Furthermore, there is significantly more uncertainty in the location of this DSE-initiating event (average of 7 μs travel time residuals), compared to others (<1.5 μs). The locations of all other DSE-initiating AEs are shown in Figure 3c.

4. Discussion

4.1. Estimates of R_C

Previous work on meter-sized laboratory samples at ~5 MPa normal stress indicated that the critical nucleation size $R_C \sim 1$ m [*Okubo and Dieterich*, 1984; *Beeler et al.*, 2012; *McLaskey and Kilgore*, 2013]. The current experiments were conducted at about 20 times higher stress levels (~100 MPa) so we estimate that R_C is about 20 times smaller. This is approximate since nucleation size is also known to be a function of fault roughness [*Okubo and Dieterich*, 1984] and loading history [*Fang et al.*, 2010; *Kaneko and Lapusta*, 2008].

If R_C is small compared to the sample size, a dynamic instability can develop on a small subset of the fault and dynamically grow, so we would expect to detect little or no premonitory creep prior to a DSE. However, if R_C is larger than the sample size, we would expect the entire sample to slip quasi-stably before accelerating into a DSE.

DSE1 shows only a single precursory AE, and precursory fault slip rate does not significantly differ from 0 (Figure 8d). The majority of the simulated fault likely remained locked prior to DSE1, which indicates that R_C was smaller than the sample dimensions. Yet DSE1 was unique. For this first slip event, lapped surfaces were likely interlocking, and there was no gouge layer. Slip during DSE1 probably produced fine gouge that effectively increased the roughness of the simulated fault and promoted premonitory slip for subsequent DSEs. Continued slip and DSEs would add to gouge thickness. For DSE2–10, we infer premonitory fault slip (Figures 8a–8c) and detect precursory AEs distributed over a large percentage of the fault (Figure 3), so

we infer that a significant portion of the fault begins to slip and weaken before the DSE occurs. We therefore estimate that the average properties of the fault yield R_C close to or larger than the sample size (i.e., ~ 100 mm), and heterogeneity of fault properties creates small brittle patches that produce the AEs, as described below.

4.2. AE Mechanics and Source Parameters

Since the recording system is absolutely calibrated (McLaskey et al., submitted manuscript, 2014), we can estimate AE moment, size, and stress drop. From Figure 6, we find that the largest AEs are $A_0 = 1\text{-}10$ V, and $M_0 = 0.3 - 3$ Nm ($M = -6.4$ to -5.7). Based on spectral estimates, such as those shown in Figure 5, we can roughly estimate corner frequency f_0 of these AEs to be 200–300 kHz. If we assume the *Brune* [1970] relationship between f_0 and source dimension $r_0 = 2.34 \times \beta/(2\pi f_0)$ and calculate stress drop $\Delta\sigma = 7/16 M_0 {r_0}^{-3}$, this implies source dimensions of 4–6 mm and stress drops of 0.6–7.5 MPa. (We assume $\beta = 3200$ m/s, since most of the wave energy arrives with the *S* wave). The smallest AEs that we analyzed had moments of 0.005 Nm or 5×10^{-3} Nm ($M = -7.6$), and f_0 was estimated to be about 1 MHz. This implies r_0 of about 1 mm and stress drops of about 2 MPa. We also detected even smaller AEs which could not be analyzed with as much detail, and we estimate their magnitudes are about $M = -8$. Sometimes we find that similar-sized AEs exhibit dissimilar f_0 which would indicate variability in stress drop, but this will be considered in a future study. In general, we find that the AE stress drops are consistent with other AE and laboratory-generated earthquakes [*Sellers et al*., 2003; *McLaskey et al*., 2014], as well as natural earthquakes of all sizes [e.g., *Abercrombie*, 1995; *Ide and Beroza*, 2001; *Imanishi and Ellsworth*, 2006].

Both the AE locations and double-couple focal mechanisms are consistent with shear slip on the simulated fault, but we estimate that AEs account for less than 2% of the premonitory fault slip that occurred in the final seconds prior each DSE (Figure 8). For example, we estimate that the fault slipped about 9 μm in the 20 s prior to DSE8. Assuming fault area $A = 0.009$ m^2, granite shear modulus $\mu = 30$ GPa, and $M_0 = \mu A \delta$, we estimate that this precursory slip contributed 2400 Nm of moment release. Total AE moment release in this time period is estimated to be 34 Nm or 1.5% of the moment release inferred from aseismic slip (see Table 1). This is consistent with previous estimates, which also indicated that AEs were associated with only a small percentage of the total rock deformation [*Lockner*, 1993]. Note, that it is not possible for us to obtain a reliable estimate of slip in the final second prior to each DSE because stress and displacement data are sampled at 1 Hz and low-pass filtered. Therefore, slip estimates reported in Table 1 are lower bounds and the 2% seismic coupling is an upper bound.

Fault slip appears to be necessary, but not sufficient, for the production of the observed AEs on these smoothly lapped granite surfaces. In addition to the low seismic coupling illustrated above, there are cases for which the fault slips in a quasi-stable way and no AEs are detected. Therefore, we infer that AEs are instabilities that may occur when stress applied to a locally brittle fault patch exceeds its strength. This brittle patch could be the sudden buckling of a force chain in a granular gouge layer [*Hartley and Behringer*, 2003; *Mair et al*., 2002]. AE could also be triggered by the brittle destruction of fault surface topography, even if the majority of the moment release is deviatoric and consistent with slip on the precut fault plane. Considering focal mechanisms, source spectra, and overall behavior, we cannot find any significant differences (other than their small size) between AEs generated on the simulated fault and larger natural earthquakes. It is worth noting that a different and less competent rock type (such as Berea sandstone) may produce AEs with different mechanisms than those produced from the fine-grained granite used in these experiments.

4.3. What Causes an AE to Cascade Up?

The weak but abrupt wave arrivals produced by the onset of the DSE (Figure 1) suggest that AEs can in fact grow or cascade up into a much larger rupture. A comparison of AEs that successfully cascade up to those that do not reveals information about the spatial variation and time history of fault strength.

One possibility is that interaction with the sample boundary triggers the sudden growth of the AE into a DSE. In this case we would expect DSE-initiating AEs to always be located near the sample boundary. But DSE3 initiated almost directly in the center of the sample (see Figure 3c). Additionally, the signals from DSE-initiating AEs significantly diverge from those of typical AEs after about 5–10 μs (15–30 mm zone of influence) regardless of their proximity to the sample edge. Therefore, we believe that interaction with the sample boundary is not what causes an AE to grow.

Another hypothesis is that local fault strength, and therefore the ability of an AE to cascade up, is primarily controlled by the topography of the interacting rock surfaces. Surfaces that have been artificially ground flat have diminished long-wavelength roughness above the corner wavelength λ_c which is related to the grit size used for grinding [*Brown and Scholz*, 1985; *Ohnaka and Kuwahara*, 1990; *Marone and Cox*, 1994]. AEs with dimensions smaller than λ_c will most likely be arrested, but AEs that become larger than λ_c are unlikely to encounter a strength barrier that will arrest their propagation. This model produces a population of event sizes that is roughly consistent with the power law which describes surface roughness (i.e., a Gutenberg-Richter distribution) [*Ide and Aochi*, 2005]. The truncation of roughness at λ_c may explain the gap in the frequency-magnitude distribution between the largest AEs, with nominal linear dimension of 5 mm, and the DSEs (see, e.g., Figure 6a and *Lei* [2012, Figure 3]).

Brown and Scholz [1985] and *Marone and Cox* [1994] estimated λ_c between 1 and 10 mm for rock surfaces lapped with 60–80 grit abrasive. The current samples were prepared with 600 grit, so we would expect λ_c to be smaller. We estimate the largest AEs to have dimensions of ~5 mm, so to be entirely consistent with this hypothesis, the fault surfaces would either have to have been roughened during DSE1 (as we expect), or our estimates of source dimensions based on the Brune relation are too large.

In many cases, it is the largest AE in a sequence that grows into a DSE (Figure 8a), consistent with the above hypothesis. In other cases, the DSE-initiating AE is neither unusually large (DSE6 and DSE8–10) nor in an unusual location (DSE8–9) (see Figures S3–S8 in the supporting information). This suggests that the fault was weakened in the final millisecond prior to a DSE and thereby allowed the AE to grow large, as described below.

4.4. Cascade Facilitated by Preslip

In 9 out of 10 cases, we find that DSEs only initiate when aseismic fault slip (preslip) is already accelerating (Figure 8). We believe that this preslip is due to the large ~100 mm nucleation of the DSE. This is consistent with the numerical models of *Noda et al*. [2013], who found that for a small instability to cascade up, the larger patch must be "ready" (i.e., it is beginning to slip and its strength is reduced). We argue that preslip does two things to facilitate a cascade. (1) It drives the smaller-scale seismicity (AEs) that could potentially cascade up and (2) it weakens the surrounding fault which makes it more susceptible to a larger rupture.

The occurrence of millimeter-sized AEs probably has only a minor effect on the weakening rate of the entire precut fault (100 mm in size) but the rapid slip associated with a seismic event such as an AE produces significant local changes in stress. If this stress exceeds the strength of the surrounding fault, the seismic event will grow. In this sense, AEs probe the local strength of the fault. Because AEs that do not cascade up occur even in the milliseconds prior to a DSE, and since many of them have sizes and locations that are comparable to the DSE-initiating AE, we interpret this as evidence that fault weakening occurred rapidly, on a time scale of hundreds of milliseconds.

Finally, accelerating aseismic slip may have a profound effect on the occurrence of AEs. For example, *McLaskey and Kilgore* [2013] showed that increased local stressing rate due to aseismic slip promoted instability (i.e., made the fault more brittle) and caused seismic waves to be radiated from fault patches which would have otherwise slipped aseismically. High local stressing rates resulting from preslip may limit the role of thermally activated failure mechanisms such as dislocation motion and slow crack growth which would otherwise allow potential AE sites to slip slowly and aseismically.

4.5. Application to Natural Faults

A consequence of the cascade-up process described above is that signals associated with DSEs have first motions that are weak but abrupt (rather than emergent or initially strong). This is also a relatively common feature of seismograms recorded from natural earthquakes of all sizes [*Beroza and Ellsworth*, 1996], so we believe that a similar cascade-up process often occurs on natural faults. *Uchide and Ide* [2010] reported that observed seismic waveforms for *M* 1.6 to *M* 6.0 earthquakes in the Parkfield area initiate abruptly and are nearly identical for the first 30 ms, consistent with the cascade model.

Despite the lack of geodetic evidence [*Roeloffs*, 2006], we expect that, in general, earthquakes initiate with preslip, generally consistent with the work of *Dieterich* [1992]. But multiscale roughness of the fault

surfaces probably provides the heterogeneity of fault strength (and brittleness) necessary to produce small ruptures that occur within the larger, tougher fault section that is slipping aseismically. Foreshocks and aftershocks are likely a manifestation of this behavior. Weak-but-abrupt initial *P* wave signatures are relatively common, and detectable foreshocks are less common, so a cascade-up process is probably a dominant mode of rupture initiation in nature.

5. Conclusions

In this work, we were able to directly compare tiny AEs to large stick-slip instabilities that rupture the entire simulated fault plane (DSEs). While the AEs have corner frequencies in the ~200–1000 kHz range, DSE corner frequencies are at most 20 kHz, and source durations are at least 50 μs. We estimated locations, focal mechanisms, source dimensions, moments, and stress drops for the AEs, which allows us to better constrain their mechanics. While some brittle process must be required for their existence, such as brittle microfracture or instability in a gouge layer, their double-couple focal mechanisms, 1–5 mm sizes, and locations suggest that they are predominantly the result of shear slip across the saw-cut fault.

We observed that in 9 of 10 cases the seismic signature of the DSEs initiates with a weak-but-abrupt onset, similar in size and shape to the premonitory AEs that occur in the seconds to milliseconds prior to the DSEs. This indicates that an AE-like instability (a DSE-initiating AE) dynamically triggers the DSE in a cascade-up process. Our results indicate that it is not an interaction with the edge of the sample that causes the AE to cascade up. AEs that cascade up are among the largest AEs recorded which suggests that it is their size relative to the roughness of the simulated fault that enables their growth.

The premonitory AEs are associated with independently measurable and mostly aseismic (>98%) premonitory fault slip that accelerates in the final 10 s before a DSE. We argue that this fault slip is the result of the nucleation process (i.e., preslip) of the DSE. Even though a cascade process is immediately responsible for the larger instability, most of the processes preparing the fault for instability are aseismic. Preslip is required to both generate the AE that could potentially cascade up, and weaken the surrounding fault in order to allow the cascade process to occur. Weak-but-abrupt wave arrivals are often observed in the seismograms of natural earthquakes, and this suggests that similar processes may occur in nature.

Acknowledgments
This paper was improved by helpful reviews by Art McGarr, Nick Beeler, Thomas Goebel, and an anonymous reviewer. Data used in this paper were acquired during laboratory experiments at the U.S. Geological Survey in Menlo Park, California. Data can be made available by the authors upon request.

References

Abercrombie, R. E. (1995), Earthquake source scaling relationships from −1 to 5 ML using seismograms recorded at 2.5-km depth, *J. Geophys. Res.*, *100*, 24,015–24,036, doi:10.1029/95JB02397.

Baumberger, T., F. Heslot, and B. Perrin (1994), Crossover from creep to inertial motion in friction dynamics, *Nature*, *367*, 544–546.

Beeler, N. M., B. Kilgore, A. McGarr, J. Fletcher, J. Evans, and S. R. Baker (2012), Observed source parameters for dynamic rupture with non-uniform initial stress and relatively high fracture energy, *J. Struct. Geol.*, *38*, 77–89.

Beroza, G. C., and W. L. Ellsworth (1996), Properties of the seismic nucleation phase, *Tectonophysics*, *261*, 209–227.

Brace, W. F., and J. D. Byerlee (1966), Stick slip as a mechanism for earthquakes, *Science*, *153*, 990–992.

Brown, S. R., and C. H. Scholz (1985), Closure of random elastic surfaces in contact, *J. Geophys. Res.*, *90*(B7), 5531–5545, doi:10.1029/JB090iB07p05531.

Brune, J. N. (1970), Tectonic stress and spectra of seismic shear waves from earthquakes, *J. Geophys. Res.*, *75*, 4997–5009, doi:10.1029/JB075i026p04997.

Dieterich, J. H. (1978), Time-dependent friction and the mechanics of stick-slip, *Pure Appl. Geophys.*, *116*, 790–806.

Dieterich, J. H. (1992), Earthquake nucleation on faults with rate- and state-dependent strength, *Tectonophysics*, *211*, 115–134.

Ellsworth, W., and G. C. Beroza (1995), Seismic evidence for an earthquake nucleation phase, *Science*, *268*, 851–855.

Fang, Z., J. H. Dieterich, and G. Xu (2010), Effect of initial conditions and loading path on earthquake nucleation, *J. Geophys. Res.*, *115*, B06313, doi:10.1029/2009JB006558.

Goebel, T., T. Becker, D. Schorlemmer, S. Stanchits, C. Sammis E. Rybacki, and G. Dresen (2012), Identifying fault heterogeneity through mapping spatial anomalies in acoustic emission statistics, *J. Geophys. Res.*, *117*, B03310, doi:10.1029/2011JB008763.

Goebel, T. H. W., T. Candela, C. G. Sammis, T. W. Becker, G. Dresen, and D. Schorlemmer (2014a), Seismic event distributions and off-fault damage during frictional sliding of saw-cut surfaces with pre-defined roughness, *Geophys. J. Int.*, *196*(1), 612–625, doi:10.1093/gji/ggt401.

Goebel, T. H. W., C. G. Sammis, T. W. Becker, G. Dresen, and D. Schorlemmer (2014b), A comparison of seismicity characteristics and fault structure in stick-slip experiments and nature, *Pure Appl. Geophys.*, doi:10.1007/s00024-013-0713-7, in press.

Harris, F. (1978), On the use of windows for harmonic analysis with discrete Fourier transform, *Proc. IEEE*, *66*(1), 51–83.

Hartley, R. R., and R. P. Behringer (2003), Logarithmic rate dependence of force networks in sheared granular materials, *Nature*, *421*, 928–931.

Ide, S., and H. Aochi (2005), Earthquakes as multiscale dynamic ruptures with heterogeneous fracture surface energy, *J. Geophys. Res.*, *110*, B11303, doi:10.1029/2004JB003591.

Ide, S., and G. Beroza (2001), Does apparent stress vary with earthquake size?, *Geophys. Res. Lett.*, *28*, 3349–3352, doi:10.1029/2001GL013106.

Imanishi, K., and W. L. Ellsworth (2006), Source scaling relationships of microearthquakes at Parkfield, CA, determined using the SAFOD Pilot Hole Seismic Array, in *Earthquakes: Radiated Energy and the Physics of Earthquake Faulting*, *Geophys. Monogr. Ser.*, vol. 170, edited by R. Abercrombie et al., pp. 81–90, AGU, Washington, D. C.

Johnson, P., B. Ferdowsi, B. Kaproth, M. Scuderi, M. Griffa, J. Carmeliet, R. Guyer, P. Y. Le Bas, D. Trugman, and C. Marone (2013), Acoustic emission and microslip precursors to stick-slip failure in sheared granular material, *Geophys. Res. Lett.*, *40*, 5627–5631, doi:10.1002/2013GL057848.

Kaneko, Y., and N. Lapusta (2008), Variability of earthquake nucleation in continuum models of rate-and-state faults and implications for aftershock rates, *J. Geophys. Res.*, *113*, B12312, doi:10.1029/2007JB005154.

Lapusta, N., and Y. Liu (2009), Three-dimensional boundary integral modeling of spontaneous earthquake sequences and aseismic slip, *J. Geophys. Res.*, *114*, B09303, doi:10.1029/2008JB005934.

Lei, X. (2012), Dragon-Kings in rock fracturing: Insights gained from rock fracture tests in the laboratory, *Eur. Phys. J. Spec. Top.*, *205*, 217–230, doi:10.1140/epjst/e2012-01572-8.

Lei, X., K. Kusunose, T. Satoh, and O. Nishizawa (2003), The hierarchical rupture process of a fault: An experimental study, *Phys. Earth. Planet. Inter.*, *137*, 213–228.

Lockner, D. A. (1993), Role of acoustic emission in the study of rock fracture, *Int. J. Rock Mech. Min. Sci. Geomech. Abstr.*, *30*, 884–899.

Mahajan, A., and M. Walworth (2001), 3-D position sensing using the differences in the time-of-flights from a wave source to various receivers, *IEEE Trans. Robot. Autom.*, *17*, 91–94.

Mair, K., K. M. Frye, and C. Marone (2002), Influence of grain characteristics on the friction of granular shear zones, *J. Geophys. Res.*, *107*(B10), 2219, doi:10.1029/2001JB000516.

Marone, C., and S. J. D. Cox (1994), Scaling of rock friction constitutive parameters: The effects of surface roughness and cumulative offset on friction of gabbro, *Pure Appl. Geophys.*, *143*, 359–86.

McGarr, A. (2012), Relating stick-slip friction experiments to earthquake source parameters, *Geophys. Res. Lett.*, *39*, L05303, doi:10.1029/2011GL050327

McLaskey, G. C., and B. D. Kilgore (2013), Foreshocks during the nucleation of stick-slip instability, *J. Geophys. Res. Solid Earth*, *118*, 2982–2997, doi:10.1002/jgrb.50232.

McLaskey, G. C., A. M. Thomas, S. D. Glaser, and R. M. Nadeau (2012), Fault healing promotes high-frequency earthquakes in laboratory experiments and on natural faults, *Nature*, *491*, 101–104, doi:10.1038/nature11512.

McLaskey, G. C., B. D. Kilgore, D. A. Lockner, and N. M. Beeler (2014), Laboratory generated M −6 earthquakes, *Pure Appl. Geophys.*, doi:10.1007/s00024-013-0772-9.

Noda, H., M. Nakatani, and T. Hori (2013), Large nucleation before large earthquakes is sometimes skipped due to cascade-up—Implications from a rate and state simulation of faults with hierarchical asperities, *J. Geophys. Res. Solid Earth*, *118*, 2924–2952, doi:10.1002/jgrb.50211.

Ohnaka, M., and Y. Kuwahara (1990), Characteristic features of local breakdown near a crack-tip in the transition zone from nucleation to unstable rupture during stick-slip shear failure, *Tectonophysics*, *175*, 197–220.

Okubo, P. G., and J. H. Dieterich (1984), Effects of physical fault properties on frictional instabilities produced on simulated faults, *J. Geophys. Res.*, *89*, 5817–5827, doi:10.1029/JB089iB07p05817.

Passelègue, F. X., A. Schubnel, S. Nielsen, H. S. Bhat, and R. Madariaga (2013), From sub-Rayleigh to supershear ruptures during stick-slip experiments on crustal rocks, *Science*, *340*(6137), 1208–1211.

Roeloffs, E. (2006), Evidence for aseismic deformation rate changes prior to earthquakes, *Annu. Rev. Earth Planet. Sci.*, *34*, 591–627.

Ruina, A. (1983), Slip instability and state variable friction laws, *J. Geophys. Res.*, *88*(B12), 10,359–10,370, doi:10.1029/JB088iB12p10359.

Salamon, M. D. G., and G. A. Wiebols (1974), Digital location of seismic events by an underground network of seismometers using the arrival times of compressional waves, *Rock Mech.*, *6*, 141–166.

Sellers, E. J., M. O. Kataka, and L. M. Linzer (2003), Source parameters of acoustic emission events and scaling with mining-induced seismicity, *J. Geophys. Res.*, *108*(B9), 2418, doi:10.1029/2001JB000670.

Stanchits, S. A., D. A. Lockner, and A. V. Ponomarev (2003), Anisotropic changes in *P*-wave velocity and attenuation during deformation and fluid infiltration of granite, *Bull. Seismol. Soc. Am.*, *93*(4), 1803–1822.

Thompson, B. D., R. P. Young, and D. A. Lockner (2005), Observations of premonitory acoustic emission and slip nucleation during a stick slip experiment in smooth faulted Westerly granite, *Geophys. Res. Lett.*, *32*, L10304, doi:10.1029/2005GL022750.

Thompson, B. D., R. P. Young, and D. A. Lockner (2009), Premonitory acoustic emissions and stick-slip in natural and smooth-faulted Westerly granite, *J. Geophys. Res.*, *114*, B02205, doi:10.1029/2008JB005753.

Uchide, T., and S. Ide (2010), Scaling of earthquake rupture growth in the Parkfield area: Self-similar growth and suppression by the finite seismogenic layer, *J. Geophys. Res.*, *115*, B11302, doi:10.1029/2009JB007122.

Weeks, J., D. Lockner, and J. Byerlee (1978), Change in *b*-values during movement on cut surfaces in granite, *Bull. Seismol. Soc. Am.*, *68*(2), 333–341.

Zang, A., C. Wagner, S. Stanchits, G. Dresen, R. Andresen, and M. Haidekker (1998), Source analysis of acoustic emissions in Aue granite cores under symmetric and asymmetric compressive loads, *Geophys. J. Int.*, *135*, 1113–1130.